ELSEVIER

Journal of Magnetism and Magnetic Materials 231 (2001) 219–230

Journal of magnetism and magnetic materials

www.elsevier.com/locate/jmmm

Coercivity limits and mechanism in nanocomposite Nd–Fe–B alloys

Er. Girt[a,b], Kannan M. Krishnan[a,*], G. Thomas[b], E. Girt[c], Z. Altounian[d]

[a] *Material Science Division, Lawrence Berkeley National Laboratory, University of California, Berkeley, CA 94720, USA*
[b] *Department of Material Science and Mineral Engineering, University of California, Berkeley, CA 94720, USA*
[c] *Department of Physics, Faculty of Natural Sciences and Mathematics, Zmaja od Bosne 35, 71000 Sarajevo, Bosnia and Herzegowina*
[d] *Department of Physics, Centre for the Physics of Materials, McGill University, 3600 University Street, Montréal, Québec, Canada H3A 2T8*

Received 17 December 1999; received in revised form 25 October 2000

Abstract

The largest coercivity in the Nd–Fe–B system was achieved by systematically tailoring the microstructure from strongly interacting $Nd_2Fe_{14}B$ grains to magnetically isolated $Nd_2Fe_{14}B$ grains in a Nd-rich matrix. The crystal structure, phase purity and magnetic properties of the Nd–Fe–B samples were extensively measured. In particular energy-filtered images, using spatially resolved measurements of inner-shell ionization edges, was critical in evaluating the particle shapes (platelets with the crystallographic *c*-axis normal to the plate), size ($\sim 100 \times 40 \times 25$ nm) and distribution. For randomly oriented, non-interacting particles, the largest observed coercivity, $\mu_0 H_c \sim 2.75$ T is $\sim 83\%$ of the theoretical limit expected for Stoner–Wohlfarth coherent rotation behavior including demagnetization effects. Initial magnetization curves of thermally demagnetized Nd–Fe–B samples show a systematic increase in susceptibility with an increase in Nd concentration as a result of a competition between contributions from strongly interacting $Nd_2Fe_{14}B$ grains with grain sizes smaller or equal to the magnetic domain size and completely isolated multidomain $Nd_2Fe_{14}B$ grains. The possible coercivity mechanisms in such Nd–Fe–B samples are discussed.

Keywords: Alloys; Coercivity; Nanocomposites; Interacting grains

1. Introduction

Coercivity mechanism in magnetic materials containing strongly interacting grains with sizes close to the critical size for single-domain particle is still not well understood [1]. These materials exhibit low initial susceptibility after thermal demagnetization and thus, it is often assumed that pinning of domain walls on the grain boundary is the dominant hardening mechanism in these materials. Attempts have been made to understand the coercivity mechanism in these materials by systematically varying the grain size of $Nd_2Fe_{14}B$ in rapidly quenched Nd–Fe–B samples [2]. The initial magnetization curve of these samples showed two steps: the first was assumed to be due to the contribution from multidomain grains

*Corresponding author. Fax: +1-510-486-5888.
E-mail addresses: EGirt@lbl.gov (K.M. Krishnan).

0304-8853/01/$ - see front matter.
PII: S0304-8853(01)00031-2

as characterized by a large initial susceptibility and the second due to the contribution from single-domain grains with characteristically low initial susceptibility [2]. However, once the magnetic moments of the grains are saturated, the demagnetization curves show a unique critical field corresponding to coercivity, $\mu_0 H_c$, which decreases by only 10% if the grain sizes change from 100 to 1000 nm. This decrease was explained by stray fields and assuming that the reversal process in the grains is controlled by the nucleation mechanism [2]. The temperature dependence of $\mu_0 H_c$ was also found to be only slightly affected by the grain size [2]. Thus, it was concluded that the magnetic reversal in saturated grains is independent of the grain size and is dominated only by one mechanism, i.e., nucleation.

The coercive field in magnetic materials strongly depends on both intrinsic magnetic properties and the microstructure of the material. In theory, the nucleation field, assuming coherent rotation of non-interacting, single domain, magnetic particles with $K_1 \gg K_2$, can be written [3] as $\mu_0 H_N = 2K_1/M_s - NJ_s$. Here K_1 and K_2 are the magnetocrystalline anisotropy constants, J_s is the spontaneous polarization and N is the demagnetization factor. For an assembly of randomly oriented, non-interacting particles the Stoner–Wohlfarth model [4] predicts that $\mu_0 H_c$ decreases to about half the value of the nucleation field for a single-domain particle. In order to obtain a microstructure with non-interacting single-domain particles, nanocomposite materials with mixtures of magnetic and non-magnetic phases have been studied [5–8]. In such nanocomposite permanent magnetic materials, values of the coercive field were found to be at least 2 times smaller than the theoretically predicted, directionally averaged, value [5–8]. This discrepancy was attributed to strong local stray fields arising at sharp edges and corners of magnetic grains, and the surface regions in magnetic grains where the anisotropy constant K_1 is reduced [5].

In order to understand the coercivity mechanism in materials with grain sizes of the order of the critical size for a single magnetic domain, and the difference between the theoretically predicted and experimentally obtained results for $\mu_0 H_c$, rapidly quenched, Nd-rich, $Nd_\delta Fe_{13.1}B$ ($2.05 \leqslant \delta \leqslant 147.6$) and $Nd_\delta Fe_{14}B$ ($\delta = 40.6$, 151.7) ribbons were prepared. The motivation was to obtain randomly oriented, single domain, $Nd_2Fe_{14}B$ particles embedded in a non-magnetic Nd matrix. By systematically changing the amount of the non-magnetic Nd matrix, the interaction between $Nd_2Fe_{14}B$ particles is expected to range from strongly magnetically interacting in $Nd_{2.05}Fe_{13.1}B$, to nearly non-interacting $Nd_2Fe_{14}B$ particles in $Nd_{147.6}Fe_{13.1}B$, and $Nd_{151.7}Fe_{14}B$ alloys. In this way the effect of the interaction between magnetic grains on the magnitude and mechanism of coercivity can be investigated. The change in the composition will have an affect on the microstructure and therefore on the magnetic properties of the Nd–Fe–B samples. Thus, in this paper we will also put an emphasis on the microstructural investigation of Nd–Fe–B using electron microscopy. Finally, $Nd_2Fe_{14}B$ was chosen because of its large magnetocrystalline anisotropy, $\mu_0 H_A > J_s$. Thus, magnetization reversal is governed by domain wall processes. Mechanisms of magnetization reversal such as curling and buckling are not energetically favorable [9] and will not be discussed in this paper.

2. Sample preparation

The $Nd_\delta Fe_{13.1}B$ ($2.05 \leqslant \delta \leqslant 147.6$) alloys were prepared by arc-melting. The ingots were melt-spun in an argon atmosphere using a Cu wheel with a surface speed of 35 m/s. The crystallization temperature of the amorphous phase in ribbons was measured by DSC using a scan rate of 40 K/min. The annealing treatments were performed in an evacuated quartz tube at annealing temperatures ranging from 723 to 923 K and annealing time between 2 min to 1 h. Structural data on the as-quenched and annealed ribbons were obtained by X-ray diffraction using $Cu\,K_\alpha$ radiation. Thermomagnetic analysis (TMA) was used for detecting Curie temperatures, T_c, of ribbons before and after annealing. Magnetization measurements at room temperature were performed with a SQUID and a vibration sample magnetometer (VSM) with a maximum external field,

$\mu_0 H_a$, up to 5.5 and 1.4 T, respectively, applied parallel to the ribbon direction. The coercivity strongly depends on the orientation of $Nd_2Fe_{14}B$ grains. Thus, to eliminate a possible contribution from the texturing of $Nd_2Fe_{14}B$ grains to the coercivity, $Nd_\delta Fe_{13.1}B$ ribbons were also ground to a powder with particle sizes below 50 μm. The powder was then mixed with an epoxy and placed between two glass slides to obtain flakes of dimensions about $7 \times 7 \times 0.4$–0.3 mm. The SQUID measurements on the powder samples were done with the field parallel to the 7×7 mm surface. The external field was corrected by the demagnetization field according to $\mu_0 H = \mu H_{ext} - NJ$, where N is the demagnetization factor and J is the polarization. N was estimated to be 0.008 for the ribbon samples and 0.04 for the powder samples using an expression valid for ellipsoids. The $M(H)$ loop of $Nd_\delta Fe_{13.1}B$ (except for $Nd_{2.05}Fe_{13.1}B$) contains contributions from the $Nd_2Fe_{14}B$ phase and the paramagnetic Nd-rich matrix. The paramagnetic contribution was determined assuming that all the Fe in $Nd_\delta Fe_{13.1}B$ reacts with Nd and B to form $Nd_2Fe_{14}B$ and that the excess Nd-rich matrix is α-Nd. The microstructure of $Nd_\delta Fe_{13.1}B$ was investigated by conventional TEM and energy filtered imaging [10,11] based on electron energy-loss spectroscopy (EELS). Quantitative chemical analyses of Nd–Fe–B samples were obtained using EELS and energy dispersive X-ray microanalysis (EDX) in a TEM.

3. Optimal annealing, structural characterization and phase purity

DSC measurements show that the crystallization temperature of the $Nd_2Fe_{14}B$ phase decreases with an increase of the Nd concentration for $\delta \leqslant 38.1$ in $Nd_\delta Fe_{13.1}B$. The same trend has been already reported for $Nd_\delta Fe_{19-\delta}B$ ($3 \leqslant \delta \leqslant 5$) [12]. Thermal scans of as-quenched $Nd_{2.05}Fe_{13.1}B$ and $Nd_{73}Fe_{25.09}B_{1.91}$ are shown in Fig. 1. For the former it shows that crystallization of the $Nd_2Fe_{14}B$ phase occurs above 850 K with the peak temperature, T_p, at 872 K, in agreement with previously reported results [13]. The latter shows

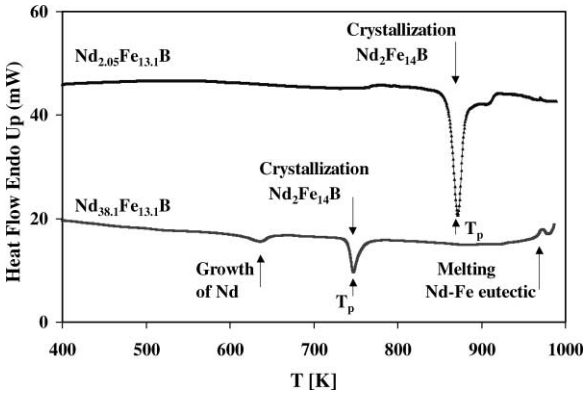

Fig. 1. DSC thermal scans of $Nd_{2.05}Fe_{13.1}B$ and $Nd_{38.1}Fe_{13.1}B$.

a broad exothermal peak at $T_p = 640$ K which corresponds to the growth of α-Nd and the main crystallization peak of $Nd_2Fe_{14}B$ at $T_p = 750$ K. The melting of the Nd–Fe eutectic was also observed above 970 K for $Nd_{73}Fe_{25.09}B_{1.91}$. The crystallization peak of $Nd_2Fe_{14}B$ in $Nd_{147.6}Fe_{25.09}B_{1.91}$ appears at the same temperature as in $Nd_{73}Fe_{25.09}B_{1.91}$. As the crystallization temperature of the $Nd_2Fe_{14}B$ phase changes with the Nd concentration, δ the annealing conditions for obtaining the $Nd_\delta Fe_{13.1}B$ samples with the optimal microstructure, i.e., with the largest coercivity, was adjusted for each composition separately. For each composition, the coercivity was also measured as a function of annealing time to obtain the optimal annealing conditions, i.e., for $Nd_{2.05}Fe_{13.1}B$, $Nd_\delta Fe_{13.1}B$ ($\delta = 3.8, 6, 8.9, 12.7$) and $Nd_\delta Fe_{13.1}B$ ($\delta = 38.1, 147.6$) ribbons they were found to be 4 min at 923 K, 2 min at 873 K and 4 min at 823 K, respectively.

X-ray diffraction analyses shows that the as-quenched samples are amorphous or partially amorphous. After optimal annealing, all the samples ($\delta > 2.05$) consist of randomly oriented $Nd_2Fe_{14}B$ particles in a α-Nd matrix. A few percent of the γ-Nd phase was also detected in the Nd–Fe–B samples [14]. For higher Nd concentrations $\delta \leqslant 38.1$, the random orientation of the $Nd_2Fe_{14}B$ grains was confirmed from the ring electron diffraction patterns together with tilting experiments. X-ray diffraction patterns of as-quenched and annealed $Nd_{12.7}Fe_{13.1}B$ are

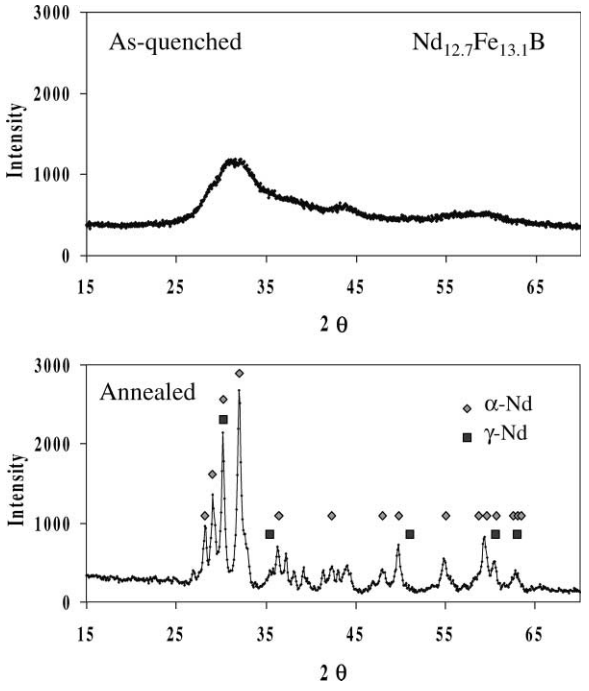

Fig. 2. X-ray diffraction patterns of the as-quenched and annealed $Nd_{12.7}Fe_{13.1}B$ samples. Diamonds and squares assign the position of the Bragg peaks of α-Nd and γ-Nd phases, respectively.

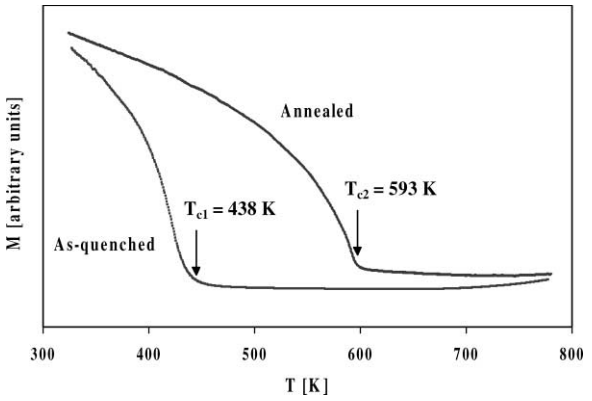

Fig. 3. TMA measurements of the as-quenched and annealed $Nd_{38.1}Fe_{13.1}B$ samples. The Curie temperatures are marked.

shown in Fig. 2. The as-quenched $Nd_{12.7}Fe_{13.1}B$ sample is amorphous and upon annealing (873 K for 2 min) crystallizes into $Nd_2Fe_{14}B$ and α-Nd/γ-Nd. The peaks corresponding to α- and γ-Nd are labeled in Fig. 2.

TMA measurements of the as-quenched and annealed $Nd_{38.1}Fe_{13.1}B$ samples (Fig. 3) show that both of them have a single magnetic (Curie point) transition [15]. For the as-quenched samples, this transition is at 438 K, and it corresponds to the amorphous phase, while for the annealed samples this transition is at 593 K corresponding to the $Nd_2Fe_{14}B$ phase. A single magnetic transition, which corresponds to the $Nd_2Fe_{14}B$ phase, was also detected by TMA in all the other optimally annealed $Nd_\delta Fe_{13.1}B$ samples.

4. Coercivity measurements

The SQUID magnetometry results for the $Nd_2Fe_{14}B$ phase in $Nd_\delta Fe_{13.1}B$ (Fig. 4) shows that $\mu_0 H_c$ increases with an increase in Nd concentration from 1.2 ± 0.03 T for $Nd_{2.05}Fe_{13.1}B$ to 2.75 ± 0.03 T for $Nd_{147.6}Fe_{13.1}B$. The error bars were estimated from measuring four different ribbon samples with the same composition. Fig. 4 shows that the discrepancy between the values of coercivity obtained for the ribbon and powder samples is small, confirming the random orientation of the $Nd_2Fe_{14}B$ grains in the ribbons. The small deviation in the Fe : B ratio does not

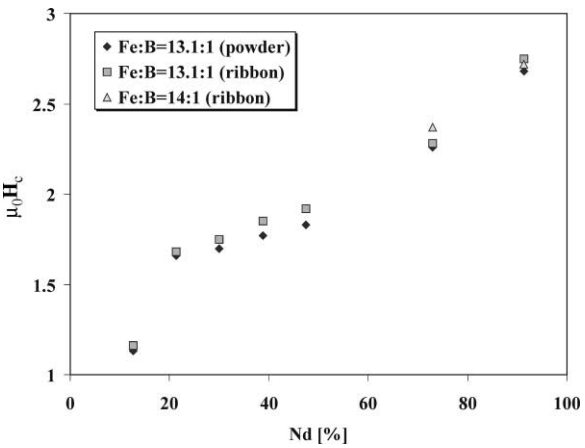

Fig. 4. The coercivity [T] of the $Nd_2Fe_{14}B$ phase as a function of Nd concentration, δ, in optimally annealed $Nd_\delta Fe_{13.1}B$ ($2.05 \leqslant \delta \leqslant 147.6$) (ribbons and powdered sample) and $Nd_\delta Fe_{14}B$ ($\delta = 40.6$, 151.7). The error in the measurements is smaller than the symbols.

have a large effect on coercivity (Fig. 4) confirming the observed trend for coercivity as a function of Nd concentration. The $J(\mu_0 H)$ measurements also show that the ratio between the saturation and remanent polarization, $J_s(\mu_0 H_{ext} = 5.5\,T)/J_r$ increases with an increase of the Nd concentration from 1.6 in $Nd_{2.05}Fe_{13.1}B$ to 1.8 in $Nd_{147.6}Fe_{13.1}B$. Using the law of approach we extrapolated the values of $J_s(\mu_0 H_{ext} \to \infty)$ for both $Nd_{2.05}Fe_{13.1}B$ and $Nd_{147.6}Fe_{13.1}B$ and found that the $J_s(\infty)/J_r$ ratio varies from 1.8 for $Nd_{2.05}Fe_{13.1}B$ to 2 in $Nd_{147.6}Fe_{13.1}B$. The latter is expected for completely uncoupled, randomly oriented magnetic particles. This confirms that we have correctly accounted for the paramagnetic contribution from the Nd-rich matrix. Hence, it is concluded that the excess Nd in $Nd_\delta Fe_{13.1}B$ forms a paramagnetic Nd-matrix, which reduces the exchange interaction between the $Nd_2Fe_{14}B$ grains.

5. Microstructural characterization: electron microscopy

The difficulties in obtaining sizes and shape distribution of $Nd_2Fe_{14}B$ grains from conventional bright field images (Fig. 5a) in a TEM were overcome by energy-filtered imaging using inner-shell ionization edges in electron energy-loss spectroscopy (Fig. 5c). This was done by selecting energy windows around the Nd $M_{4,5}$ edge for mapping Nd and energy windows around the Fe $L_{2,3}$ edge for mapping Fe. For each map, one energy window was positioned at the onset of the characteristic edge to obtain the signal due to the energy-loss of the transmitted electrons (post-edge image) and two energy windows before the edge to extrapolate the background below the ionization edge (pre-edge 1 and pre-edge 2 images) [16]. The widths of the energy windows were 20 eV for Fe and 30 eV for Nd. The Nd and Fe jump ratio images, obtained by dividing the post-edge by the pre-edge 2 image [16], are shown in Fig. 5e and f, respectively. These images clearly delineate *all* the $Nd_2Fe_{14}B$ grains that are embedded in the Nd-rich matrix. The $Nd_2Fe_{14}B$ grains are dark in the Nd map (Fig. 5e), and bright in the Fe map (Fig. 5f). Electron energy-loss spectra from a $Nd_2Fe_{14}B$ grain and Nd matrix, obtained using a focussed beam (10 nm in diameter) are shown in Fig. 5c and indicate the presence of Fe only in the $Nd_2Fe_{14}B$ grains. As expected, Nd was found in both particles and matrix. The Fe/Nd ratio in $Nd_{147.6}Fe_{13.1}B$ was quantitatively determined by EDX (Fig. 5d). The analyses show that the Fe/Nd ratio across grain A (Fig. 5e) is 86/14, consistent with the composition of $Nd_2Fe_{14}B$. The matrix consists mainly of Nd in agreement with electron energy-loss spectra, i.e., Fe/Nd = 4/96. The area enclosed by the dashed box in Fig. 5e was tilted in two different directions defined by the angles (α, β), $(30, 0)$, $(0, 30)$, $(-30, 0)$ and $(0, -30)$, as shown in Fig. 5h. From such tilting measurements of a large number of particles it was confirmed that the $Nd_2Fe_{14}B$ grains are platelets with an average size of $a \times b \times c = 100 \times 40 \times 25$ nm. A high resolution lattice image of a representative $Nd_2Fe_{14}B$ grain in optimally annealed $Nd_{147.6}Fe_{13.1}B$ is shown in Fig. 6 and confirms that the shortest side of the plate is along the crystallographic *c*-axis. The single crystal diffraction pattern from this particle can be indexed as the [1 1 0] zone axis of the tetragonal $Nd_2Fe_{14}B$ crystal. Fig. 6 also shows that some of the edges/corners of the $Nd_2Fe_{14}B$ grain are smooth, minimizing the strong local stray fields arising from sharp edges/corners and increasing the coercivity.

6. Coercivity limits

For such randomly oriented, non-interacting, single-domain, magnetic particles, the coercivity calculated from the Stoner–Wohlfarth model [2] should be equal to about half of the nucleation field $\mu_0 H_c \approx 0.5\,\mu_0 H_N$. Since, in $Nd_2Fe_{14}B$ at 290 K, $K_1 > 4K_2$, the coercivity can be calculated [17] as

$$\mu_0 H_c = 0.5\,\mu_0 H_N = (K_1 + K_2)/M_s - 0.5(N_\parallel - N_\perp)J_s, \quad (1)$$

where $N_\parallel$ and $N_\perp$ are the demagnetization factors parallel and perpendicular to the *c*-axis of the $Nd_2Fe_{14}B$ platelets. K_1, K_2, and J_s values of $Nd_2Fe_{14}B$ are taken from the literature [18]. As a first approximation, $N_\parallel$, and $N_\perp$ were calculated

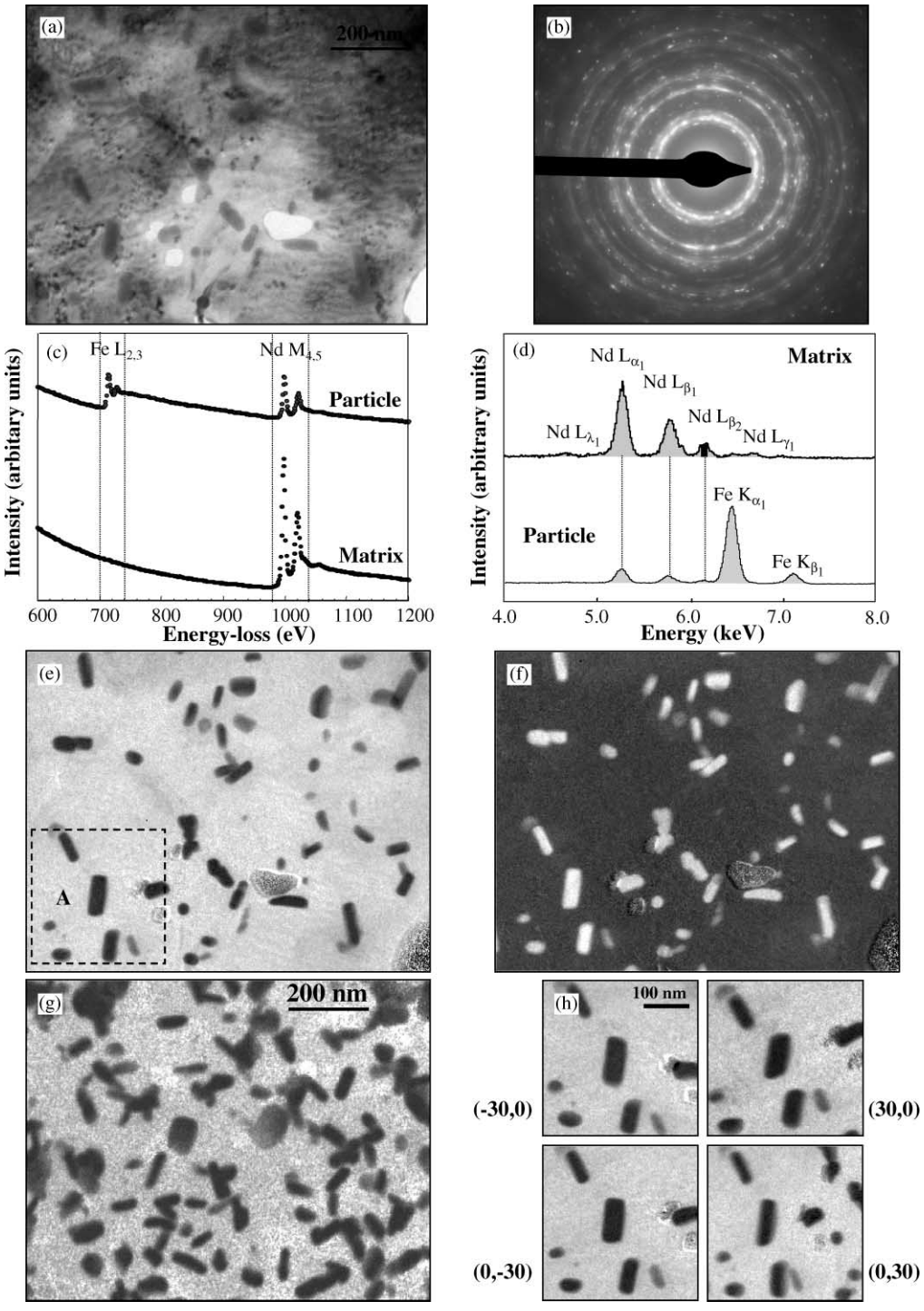

Fig. 5. (a) Bright field image and (b) selective area diffraction pattern. (c) Electron energy-loss spectra from matrix and particle, (d) energy dispersive X-ray microanalysis of matrix and particle, (e) Nd jump ratio map, (f) Fe jump ratio map, (g) Nd jump ratio map of $Nd_{38.1}Fe_{13.1}B$, (h) area assigned by the dashed line in Fig. 2(e) tilted in two different directions defined with angles (α, β): $(30, 0)$, $(0, 30)$, $(-30, 0)$ and $(0, -30)$ of $Nd_{147.6}Fe_{13.1}B$.

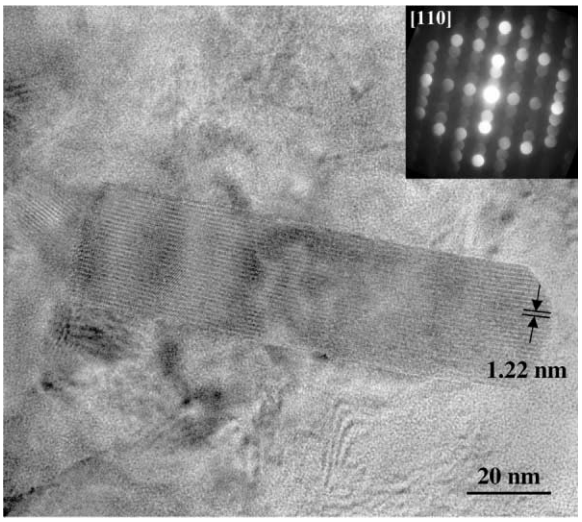

Fig. 6. Bright field image of $Nd_2Fe_{14}B$ grain in optimally annealed $Nd_{147.6}Fe_{13.1}B$. The single crystal diffraction pattern, indexed as the [1 1 0] zone axis of $Nd_2Fe_{14}B$, is presented in the upper right corner. The spacing between the rows of atoms along the c-axis of $Nd_2Fe_{14}B$ is 1.22 nm.

assuming that the $Nd_2Fe_{14}B$ grains in $Nd_{147.6}Fe_{13.1}B$ are ellipsoids with axes $a = 20$, $b = 50$ and $c = 12.5$ nm [19]. It follows from Eq. (1) that the coercivity of the $Nd_2Fe_{14}B$ grains in $Nd_{147.6}Fe_{13.1}B$ should be equal to $\mu_0 H_c = 3.33$ T. Thus, the measured coercivity of the $Nd_2Fe_{14}B$ grains in $Nd_{147.6}Fe_{13.1}B$ is about 83% of the theoretical value of coercivity obtained from the Stoner–Wohlfarth model for an assembly of randomly oriented, non-interacting, single-domain particles.

In the optimally annealed, rapidly quenched Nd–Fe–B samples the $Nd_2Fe_{14}B$ grains are randomly distributed in the Nd-rich matrix. Thus, the probability that two or more $Nd_2Fe_{14}B$ grains in the Nd–Fe–B samples are in direct contact will decrease with an increase in Nd concentration, δ. follows that in order to obtain completely isolated $Nd_2Fe_{14}B$ grains the amount of the Nd-rich matrix has to be large. This is in agreement with the energy-filtered image of the optimally annealed $Nd_{38.1}Fe_{13.1}B$ sample (Fig. 5g) which shows that a significant number of the $Nd_2Fe_{14}B$ grains are still in direct contact. On the other hand, the energy-filtered images of the optimally annealed $Nd_{147.6}Fe_{13.1}B$ sample, Fig. 5e, show that the majority of the $Nd_2Fe_{14}B$ grains are completely isolated within the non-magnetic Nd-rich matrix. Moreover, the shape and size of the $Nd_2Fe_{14}B$ grains in the optimally annealed $Nd_{38.1}Fe_{13.1}B$ and $Nd_{147.6}Fe_{13.1}B$ are similar. Since the difference in coercivity in these two samples is ~ 0.4 T, it follows that the magnetic interaction between the $Nd_2Fe_{14}B$ grains plays a key role in controlling the coercivity mechanism. If the single crystal $Nd_2Fe_{14}B$ grains (without inhomogenities which serve as pinning centers) are completely isolated as in $Nd_{147.6}Fe_{13.1}B$ (Figs. 5e and 6), and assuming a uniform grain size distribution, coercivity can be estimated by averaging the nucleation fields of all $Nd_2Fe_{14}B$ grains. However, if a reverse magnetic domain nucleates in one grain in the sample with strongly interacting single crystal $Nd_2Fe_{14}B$ grains, as in $Nd_{2.05}Fe_{13.1}B$ (Fig. 7), the magnetic domain will propagate throughout the sample by the nucleation of reverse magnetic domains in the adjacent particles. This assumes a strong positive interaction between the $Nd_2Fe_{14}B$ grains in $Nd_{2.05}Fe_{13.1}B$ presumably due to the exchange interaction between $Nd_2Fe_{14}B$ grains. Thus, in samples with strong positive interaction between grains a lower coercivity is expected.

The field required for nucleating magnetic domains in $Nd_2Fe_{14}B$ grains with surface defects or sharp corners/edges is much lower than the nucleation field expected from the magnetocrystalline anisotropy of the magnetic grain [20]. Fig. 7 show that the $Nd_2Fe_{14}B$ grains in $Nd_{2.05}Fe_{13.1}B$ have sharp edges/corners also accounting for the observed lower coercivity in this sample. Detailed micromagnetic modeling of coercivity, including interparticle interactions, based on the microstructural parameters of our Nd–Fe–B samples is in progress.

7. Coercivity mechanism

In general, coercivity mechanism is determined by the microstructure of magnetic materials. In permanent magnetic materials with large magnetocrystalline anisotropy, it is current practice to use the initial magnetization curve as a good

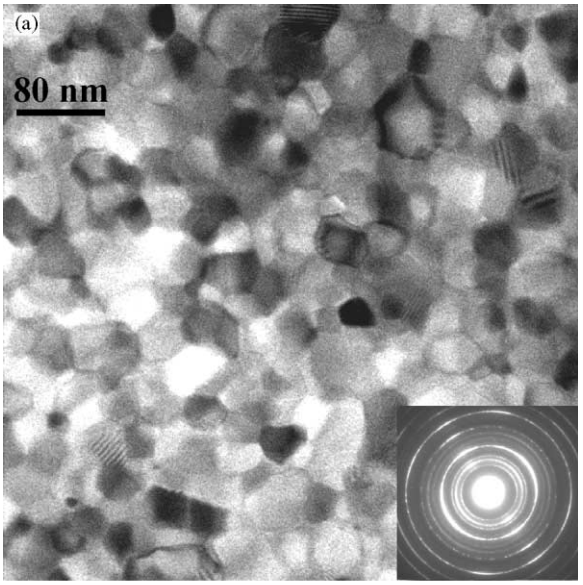

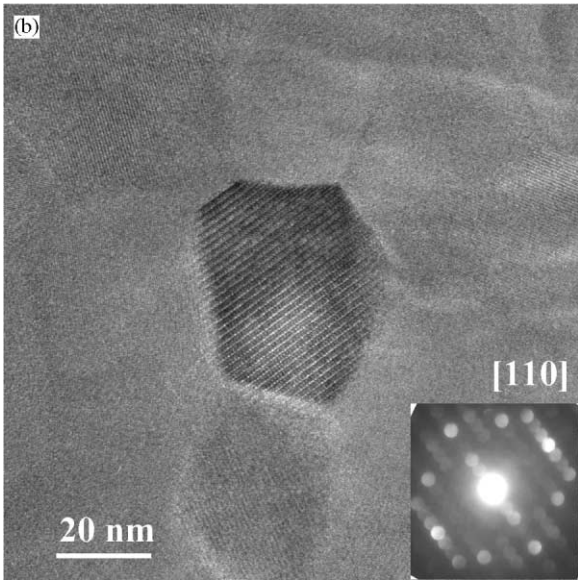

Fig. 7. Bright field image of (a) $Nd_{2.05}Fe_{13.1}B$ and (b) single crystal $Nd_2Fe_{14}B$ grain. The single crystal diffraction pattern, indexed as the [1 1 0] zone axis of $Nd_2Fe_{14}B$, is presented in the bottom right corner.

indicator of the type of coercivity mechanism, a high initial susceptibility is called 'nucleation' and a low initial susceptibility is called a 'pinning' mechanism. For thermally demagnetized samples

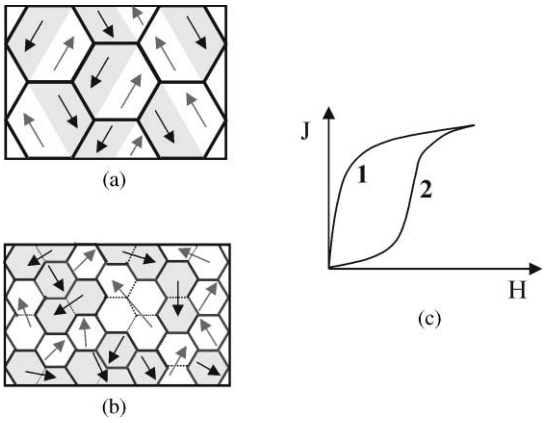

Fig. 8. Coercivity mechanism and expected behavior of the initial magnetization curve in permanent magnetic materials with a large magnetocrystalline anisotropy.

the role of microstructure in defining the coercivity mechanism can be discussed depending on the grain size (d) relative to the critical size for single-domain particle (d_{sd}). For $d > d_{sd}$, assuming a multidomain magnetic structure, if the grains do not contain inhomogenities or pinning centers, the initial susceptibility of the samples will be large, Fig. 8c (curve 1), due to the free movement of the Bloch walls throughout the grain. In this case the field required to remove Bloch walls from the grains is $\mu_0 H_{sat} = N_g J_s$ (N_g demagnetization factor of the grains and J_s their saturation magnetization) and the magnetization reversal is nucleation controlled. On the other hand, if the grains contain inhomogenities the Bloch walls are pinned at the inhomogenities in the grains (provided that the wall energy at inhomogenities is lower than in the surrounding matrix). Thus, in order to displace the Bloch walls the external field has to exceed the pinning field, $\mu_0 H_p$ and the initial susceptibility of the samples is low, Fig. 8c (curve 2). In this case, the magnetization reversal is controlled by the dominant process, $|\mu_0 H_n| > |\mu_0 H_p|$ nucleation or $|\mu_0 H_p| > |\mu_0 H_n|$ pinning. Now, let us assume that the grain sizes are smaller than or equal to the critical size for single domain $d \leqslant d_{sd}$. The initial susceptibility will always be low (curve 2) and independent of the inhomogenities contained within the grain. Thus, the initial curve is not a

good indicator of the coercivity mechanism. For interacting grains, in addition to some grains being single domains, many grains together can form a region of parallel magnetization [21]. The crucial question is whether the formation of these regions is due to the exchange or stray field coupling. If it is due to the exchange interaction, the domain wall could form along the grain boundaries, and the pinning mechanism may play an important role in controlling magnetization reversal. However, if regions of parallel magnetization are due to the stray field coupling magnetization reversal is controlled by nucleation mechanism [2]. Imaging magnetic domains may provide evidence for the precise determination of the coercivity mechanism.

From this discussion it is obvious that in order to determine the coercivity mechanism in these Nd–Fe–B samples, the critical size for single-domain $Nd_2Fe_{14}B$ grains has to be calculated. Consider the magnetization state of an isolated ferromagnetic grain in a zero magnetic field. The magnetostatic energy, E_M (due to the dipole field of the grain) is reduced by allowing a non-uniform magnetization state. Exchange interactions and anisotropy energy favor a uniform magnetization state, i.e., tend to align the magnetic moments along a unique direction. The energy balance determines the critical size for which the grain is in the uniformly magnetized state [22,23]. For a particle with high magnetocrystalline anisotropy, as in the case of $Nd_2Fe_{14}B$, the non-uniform magnetization state is a multidomain state. In a simple approach Kittel [22] assumed that E_M of a two domain state is half of the uniform magnetization state, i.e., $E_M = 1/2\ E_M + E_W$, where E_W is the energy of the domain wall. Then, for a spherical grain the critical radius for a uniformly magnetized state is $R = 9\mu_0\sigma_W/J_s^2$ ($R = 75-130$ nm assuming $\sigma_W = 17-45\,mJ/m^2$ for $Nd_2Fe_{14}B$) where σ_W is the domain wall energy per unit area and J_s is the saturation polarization. Using the same procedure the longest side, a, of the $Nd_2Fe_{14}B$ platelets (Fig. 6) is found to be $a = 4\mu_0\sigma_W/NJ_s^2$ ($a = 56-148$ nm assuming $\sigma_W = 17-45\,mJ/m^2$, N is demagnetizing factor for the plate, $E_M = 1/2\,NJ_sV/\mu_0$, V is volume of the plate). In this calculation it was assumed that the domain wall is formed perpendicular to the longest side, a, of the platelet to reduce the area of the domain wall. Then, the b and c dimensions can be calculated assuming the same ratio between a, b and c, observed for the average $Nd_2Fe_{14}B$ grain in $Nd_{147.6}Fe_{13.1}B$ ($a/b/c = 10/4/2.5$). Thus, the critical size for single-domain $Nd_2Fe_{14}B$ platelets is of the same order as the $Nd_2Fe_{14}B$ grains observed in $Nd_{147.6}Fe_{13.1}B$ (Fig. 6). The $Nd_2Fe_{14}B$ grains in $Nd_{2.05}Fe_{13.1}B$ have polyhedral shape (Fig. 7) and the calculation of critical size for the single domain is not trivial. Assuming that the $Nd_2Fe_{14}B$ grains are spheres the average radius of the $Nd_2Fe_{14}B$ grains is found to be 25 nm (Fig. 7), and is much smaller than the critical size for the single-domain grains, $R = 75-130$ nm.

8. Experimental results

Initial magnetization curves of thermally demagnetized $Nd_\delta Fe_{13.1}B$ samples are presented in Fig. 9. The results show systematic change from a single-step behavior with low initial susceptibility for $Nd_{2.05}Fe_{13.1}B$, through two-step behavior, to a single-step behavior with large initial susceptibility for $Nd_{147.6}Fe_{13.1}B$. As was discussed above, the initial magnetization curve observed for $Nd_{147.6}Fe_{13.1}B$ is expected only for multi-domain magnetic grains where the magnetization process is governed by domain displacements. The $Nd_2Fe_{14}B$ grains are defect free (Fig. 6) (without inhomogenities which could serve as pinning centers for magnetic domains) and therefore the field required to remove Bloch walls from the grains is $\mu_0 H_{sa} = N_g J_s = (N_{\|} - N_{\perp})J_s = 0.94$ T. The minor hysteresis loop measurements (Fig. 9a) show that the coercivity of $Nd_{147.6}Fe_{13.1}B$ samples increases very steeply for $\mu_0 H_{ext} \geqslant 0.2$ T approaching the coercive field, $\mu_0 H_c$, at 1.2 T. The saturation field of 1.2 T is comparable with 0.94 T assumed in Eq. (1) due to the shape anisotropy of the particles. Thus, the $Nd_2Fe_{14}B$ grains in the $Nd_{147.6}Fe_{13.1}B$ sample have multidomain structure and magnetization reversal is controlled by the nucleation mechanism only. The shape and size of the $Nd_2Fe_{14}B$ grains in the $Nd_{147.6}Fe_{13.1}B$ and $Nd_{38.1}Fe_{13.1}B$ samples are similar (Fig. 5e and Fig. 5g). The $Nd_2Fe_{14}B$ grains in the $Nd_{38.1}Fe_{13.1}B$

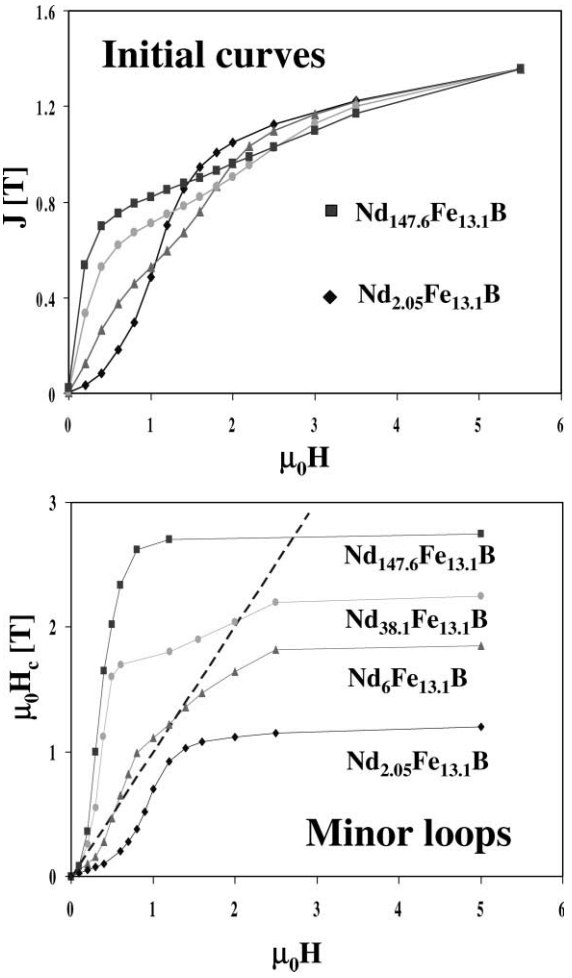

Fig. 9. (a) Initial magnetization curves and (b) minor loops (coercivity field, $\mu_0 H_c$, [T], as a function of applied field, $\mu_0 H$ [T]) of thermally demagnetized $Nd_\delta Fe_{13.1}B$. The coercivity field, $\mu_0 H_c$, is equal to the applied field, $\mu_0 H$, along the dashed line.

sample are also defect free. However, for the $Nd_{38.1}Fe_{13.1}B$ sample the initial susceptibility and minor hysteresis loop measurements show two-step behavior indicating that, beside the $Nd_2Fe_{14}B$ grains with multidomain magnetic structure, there are also $Nd_2Fe_{14}B$ grains with a single-domain magnetic structure. If the Nd concentration in the $Nd_\delta Fe_{13.1}B$ samples decreases the probability that two or more $Nd_2Fe_{14}B$ grains are in direct contact increases. It has been shown that the stray field energy of magnetic grains with uniaxial anisotropy is reduced if they are in direct contact [24]. So for grains which are in direct contact, the critical size of the single-domain grain will increase. This could explain why some of the $Nd_2Fe_{14}B$ grains in the $Nd_{38.1}Fe_{13.1}B$ sample have a single-domain structure. As discussed, the low initial susceptibility in the $Nd_{2.05}Fe_{13.1}B$ sample is not a good indicator of the coercivity mechanism since the $Nd_2Fe_{14}B$ grains are smaller than the critical size for single-domains. Minor hysteresis loops of $Nd_{2.05}Fe_{13.1}B$ samples (Fig. 9b) show that the coercivity increases very slowly if the external field, $\mu_0 H_{ext}$, is smaller than 0.6 T and then increases steeply approaching the coercive field, $\mu_0 H_c$, at 2.5 T. It is often assumed that if the field required to recover full $M(H)$ loop is larger than the coercivity field the magnetization reversal is controlled by pinning mechanism. However, this assumption is in general not valid. In the case of randomly oriented, magnetically isolated single-domain $Nd_2Fe_{14}B$ grains the field required to saturate all magnetic moments is equal to the anisotropy field, $\mu_0 H_A > \mu_0 H_c$. Thus, the low initial susceptibility in the $Nd_{2.05}Fe_{13.1}B$ sample confirms that the grain size of $Nd_2Fe_{14}B$ grains is smaller or equal to the single-domain size of the $Nd_2Fe_{14}B$ grains and also opens possibility that pinning mechanism plays an important role in controlling magnetization reversal.

Field demagnetized samples are obtained by systematically reducing applied magnetic fields of alternating polarity at a temperature below T_c of $Nd_2Fe_{14}B$. In this way domain walls can be expelled out of the $Nd_2Fe_{14}B$ grains to obtain single-domain $Nd_2Fe_{14}B$ grains while keeping zero net magnetization in the sample. The initial magnetization curve of thermally and field demagnetized $Nd_{2.05}Fe_{13.1}B$ samples (Fig. 10) show the same behavior. This suggests that the magnetic domain structure in $Nd_{2.05}Fe_{13.1}B$ samples does not change with the way the samples are demagnetized. Thus, the $Nd_2Fe_{14}B$ grains in $Nd_{2.05}Fe_{13.1}B$ samples do not have a multidomain magnetic structure. On the other hand, the initial magnetization curve of thermally- and field-demagnetized samples of $Nd_{147.6}Fe_{13.1}B$ have a completely different behavior. Thermally demagnetized samples exhibit large initial susceptibility while field demagnetized samples exhibit low

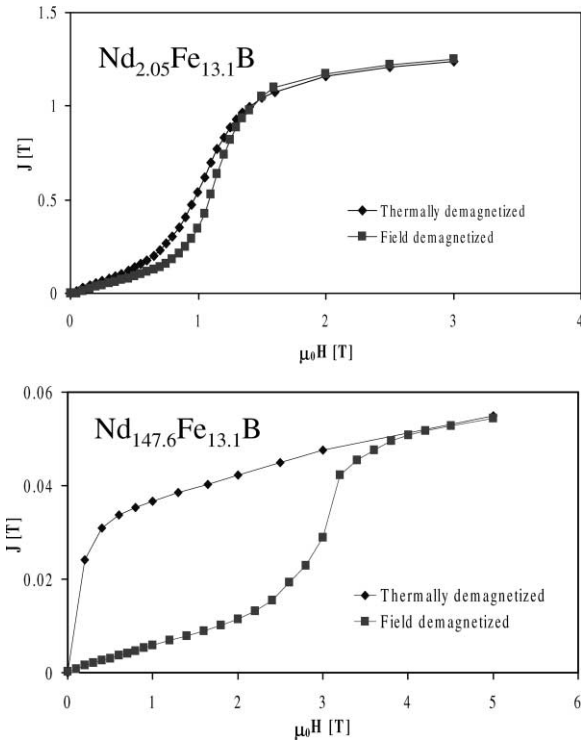

Fig. 10. The initial magnetization curves of thermally and field demagnetized $Nd_{2.05}Fe_{13.1}B$ and $Nd_{147.6}Fe_{13.1}B$ samples.

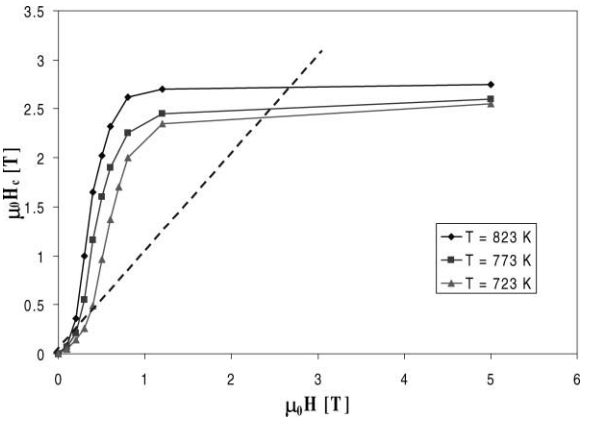

Fig. 11. Minor loops of $Nd_{147.6}Fe_{13.1}B$ annealed at 823, 873 and 923 K (optimally annealed) for 4 min. The coercivity field, $\mu_0 H_c$, is equal to the applied field, $\mu_0 H$, along the dashed line.

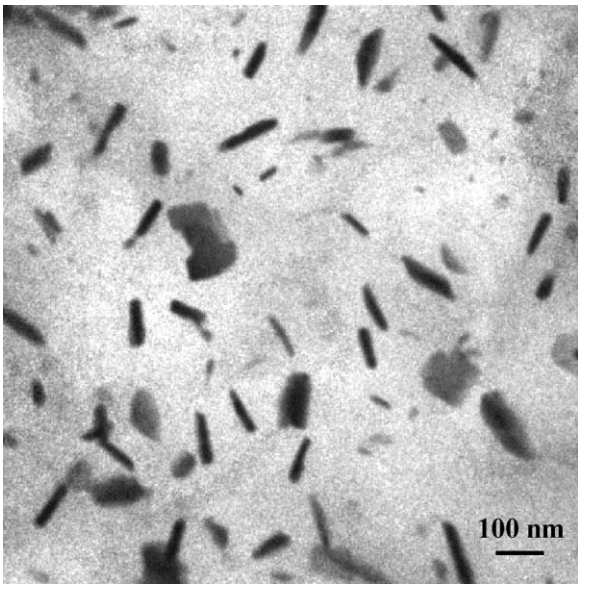

Fig. 12. The energy filtered image of $Nd_{147.6}Fe_{13.1}B$ annealed at 723 K.

initial susceptibility. This difference is due to the different magnetic structure of the $Nd_2Fe_{14}B$ grains in thermally and field demagnetized $Nd_{147.6}Fe_{13.1}B$ samples, i.e., the $Nd_2Fe_{14}B$ grains in the thermally demagnetized $Nd_{147.6}Fe_{13.1}B$ samples have a multidomain magnetic structure while the $Nd_2Fe_{14}B$ grains in the field demagnetized $Nd_{147.6}Fe_{13.1}B$ samples have a single-domain magnetic structure.

A set of minor loop measurements was also performed on $Nd_{147.6}Fe_{13.1}B$ samples annealed at 723 and 773 K for 4 min. By reducing the annealing temperature the average size of the $Nd_2Fe_{14}B$ grains is expected to decrease. The results also confirm the multidomain character of $Nd_2Fe_{14}B$ grains (Fig. 11) present in these samples. Fig. 11 also shows that the coercivity of $Nd_2Fe_{14}B$ decreases as the annealing temperature decreases. The energy filtered image of $Nd_{147.6}Fe_{13.1}B$ ribbons annealed at 723 K (Fig. 12) show that the $Nd_2Fe_{14}B$ grains are platelets, thinner in the direction perpendicular to the plate than $Nd_2Fe_{14}B$ grains in $Nd_{147.6}Fe_{13.1}B$ annealed at 823 K (Fig. 5e). $Nd_2Fe_{14}B$ grains in $Nd_{147.6}Fe_{13.1}B$ annealed at 723 K will have larger shape anisotropy and therefore a lower coercivity as predicted by Eq. (1). The decrease in the thickness of the $Nd_2Fe_{14}B$ grains in $Nd_{147.6}Fe_{13.1}B$ samples

annealed at 723 K will not change the magnetization state of the grain as long as the length of the longest side a of the platelet stays the same. Investigations of the initial magnetization state of thermally demagnetized $Nd_2Fe_{14}B$ grains using Lorentz microscopy and micromagnetic modeling of the magnetic state of $Nd_2Fe_{14}B$ grains in the paramagnetic Nd-rich matrix are in progress.

9. Conclusion

By systematically changing the Nd concentration in Nd–Fe–B alloys and appropriate annealing the microstructure was tailored from strongly interacting $Nd_2Fe_{14}B$ grains to magnetically isolated single-domain $Nd_2Fe_{14}B$ grains. The change in microstructure, i.e., the change in interaction between $Nd_2Fe_{14}B$ grains was found to have a large effect on the magnitude and mechanism of coercivity:

Coercivity increases with an increase of the Nd concentration from 1.25 T in $Nd_{2.05}Fe_{13.1}B$ to 2.75 T in $Nd_{147.6}Fe_{13.1}B$ at 290 K.

The initial magnetization of thermally demagnetized $Nd_{2.05}Fe_{13.1}B$ samples changes with an increase in Nd concentration due to the multidomain nature of the isolated $Nd_2Fe_{14}B$ platelets.

In $Nd_{147.6}Fe_{13.1}B$ the magnetization reversal is nucleation controlled. The coercivity mechanism in the samples with lower Nd concentration is not conclusive.

For nearly isolated $Nd_2Fe_{14}B$ in $Nd_{147.6}Fe_{13.1}B$ the values of coercivity are about 83% of the ideal value of coercivity obtained from the Stoner–Wohlfarth model and it is the largest value of coercivity so far reported for the $Nd_2Fe_{14}B$ phase.

Acknowledgements

This work was supported by the Director, Office of Energy Research, Office of Basic Energy Sciences, Materials Sciences Division of the US Department of Energy, under Contract No. DE-AC03-76SF00098. The authors would like to thank Dr. Wenquan Guo for performing DSC and TGA measurements, C. Echer, C. Nelson and J. Turner for assistance with electron microscopy measurements and T. Schrefl and David Crew for helpful discussions.

References

[1] J.J. Croat, J.F. Herbst, R.W. Lee, F.E. Pinkerton, J. Appl. Phys. 55 (1984) 2078.
[2] M. Grönefeld, H. Kronmüller, J. Magn. Magn. Mater. 88 (1990) L267.
[3] W.F. Brown, Rev. Mod. Phys. 17 (1945) 15.
[4] E.C. Stoner, E.P. Wohlfarth, Philos. Trans. Roy. Soc. London A 240 (1948) 599.
[5] M. Seeger, D. Köhler, H. Kronmüller, J. Magn. Magn. Mater. 130 (1994) 165.
[6] W.B. Muir, Z. Altounian, Tu Guo-hua and Chen Wanrong, J. Magn. Magn. Mater. 81 (1989) 168.
[7] V. Villas-Boas, F.P. Missell, G. Schneider, Q. Lu, D. Givord, Solid State Commun. 74 (1990) 683.
[8] G. Martinek, H. Kronmüller, S. Hirosawa, J. Magn. Magn. Mater. 89 (1990) 369.
[9] H. Fijlstra, Ferromagnetic Materials, Vol. 3, 1982.
[10] K.M. Krishnan, Er. Girt, G. Thomas, C. Nelson, Hofer, Microsc. Microanal. 5 (1999) 26.
[11] Er. Girt, K.M. Krishnan, G. Thomas, Z. Altounian, M. Dikeakos, J. Appl. Phys., in press.
[12] L.X. Liao, Z. Altounian, J. Appl. Phys. 66 (1989) 768.
[13] Jha, H.A. Davies, R.A. Buckley, J. Magn. Magn. Mater. 80, (1989) 109.
[14] Er. Girt, K.M. Krishnan, G. Thomas, Z. Altounian, C. Echer, Proceeding of the MRS Meeting, Spring 1999, in press.
[15] Er. Girt, K.M. Krishnan, G. Thomas, Z. Altounian, Appl. Phys. Lett. 76 (2000) 1746.
[16] F. Hoffer, P. Warbichler, W. Grogger, G. Kothleitner, Microsc. Anal. November (1995) 11.
[17] G. Martinek, H. Kronmüller, J. Magn. Magn. Mater. 86 (1990) 177.
[18] S. Hock, H. Kronmüller, in: Proceedings of the 5th International Symposium of Magnetic Anisotropy and Coercivity in Rare Earth-Transition Metal Alloys, Vol. 275, Bad Soden, Germany, 1987.
[19] J.A. Osborn, Phys. Rev. B 67 (1945) 351.
[20] H.F. Schmidts, Kronmüller, J. Magn. Magn. Mater. 94 (1991) 220.
[21] R.K. Mishra, R.W. Lee, Appl. Phys. Lett. 48 (1986) 733.
[22] C. Kittel, Rev. Mod. Phys. 21 (1949) 541.
[23] W.F. Brown, Ann. New York Acad. Sci. 147 (1969) 463.
[24] S. Chikazumi, in: Physics of Magnetism, John Wiley, New York, 1964, p. 234.